A Comparative Study of Magnetic Current Sensor Technologies with Experimental Evaluation Across Time, Frequency, and Impedance Domains

B.Sc Kaan Ilhan, M.Sc Eyke Aufderheide

***Abstract*—This work presents a comparative study of magnetic current transducer technologies, including Hall-effect, tunneling magneto-resistive (TMR) and anisotropic magneto-resistive (AMR) sensors. The analysis includes both theoretical operating principles and practical performance evaluations. Sensors are tested using their respective manufacturer-supplied evaluation boards to ensure optimal layout, thermal behavior, and noise characteristics. In addition to the evaluation boards, a custom high-voltage analog PCB is developed for certain sensor types to enable isolated measurement of three-phase currents up to 130 A under phase-to-phase voltages of 1000 V_{RMS}.**

The experimental evaluation includes DC output characterization, oscilloscope-based time-domain analysis, frequency-domain analysis (FFT noise spectrum), and AC impedance measurement via frequency sweep. The target application is a three-phase SiC inverter for motor drive applications. The study assesses the suitability of each sensing technology for providing accurate, isolated current measurement under fast-switching conditions.

***Index Terms*—Current transducers, Hall effect, TMR, AMR, DC Characterization, FFT, impedance measurement, three-phase inverter.**

I. Introduction

ACCURATE current measurement is essential in power electronic systems for enabling control, protection, and energy monitoring. With the increasing adoption of wide bandgap (WBG) semiconductors such as silicon carbide (SiC) and gallium nitride (GaN), modern converter systems can switch at MHz-range frequencies, demanding fast and precise current transducers [1].

Historically, various magnetic field sensing technologies have been deployed across applications ranging from angle detection and current measurement to switching and encoding. Among them, Hall-effect sensors have been the most widely adopted since their discovery. However, as system demands evolve in respect to sensitivity, bandwidth, thermal stability, and power efficiency, Hall-effect technology is approaching its performance limits [2].

To address these limitations, sensor manufacturers are transitioning toward advanced magnetoresistive technologies, especially TMR. TMR sensors, as a successor to AMR and giant magnetoresistive (GMR) approaches, offer improved performance metrics while remaining suitable for CMOS integration [2]. Each technology presents trade-offs in bandwidth, linearity, noise, and implementation complexity [1].

This paper evaluates three magnetic current transducer technologies under test conditions for high-speed inverter applications. By combining theoretical background with experimental analysis, the study aims to assess these sensors' practical suitability for use in isolated high current and high voltage measurements.

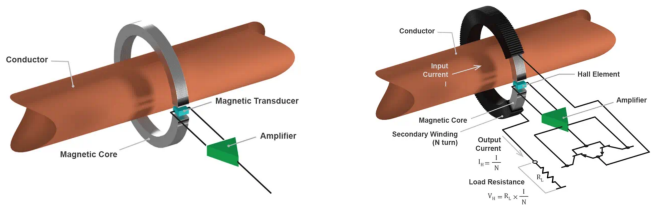

(a) Open-loop Hall-effect sensor structure [3].

(b) Closed-loop Hall-effect sensor structure [3].

Fig. 1: Hall-effect sensor topologies.

II. Magnetic Current Sensor Technologies

A. Hall-Effect Sensors

Hall-Effect Sensors rely on the Lorentz force acting on moving charges. They operate by current-carrying conductors. A Hall element is typically positioned in the air gap of a ferromagnetic core to sense the perpendicular magnetic field. This field induces a Hall voltage across the element, which is then amplified and converted into an output voltage proportional to the current [3].

Two main topologies exist for Hall-based current sensing: *open-loop* and *closed-loop*. These differ primarily in how they handle the magnetic field sensing and feedback, as illustrated in Fig. 1. In an *open-loop* configuration (Fig. 1a), the sensor directly amplifies the Hall voltage. While this design is compact and cost-effective, it is susceptible to sensitivity drift and nonlinearity due to temperature and mechanical stress effects. In contrast, a *closed-loop* Hall-effect sensor (Fig. 1b) uses a compensation/feedback coil to actively cancel the magnetic field at the Hall element. The system drives current through the coil until the net magnetic field is zero. This compensation current required to achieve the magnetic balance is measured across a sensing resistor to yield an output voltage proportional to the primary current. This method eliminate the sensitivity error and tolerances associated with the Hall sensor IC and therefore improves linearity and and frequency response [4]. However, Closed-loop sensors require additional components, including the coil and high-power amplifiers. They also consume more power, occupy more PCB space, and increase cost compared to *open-loop* designs. While closed-loop sensors

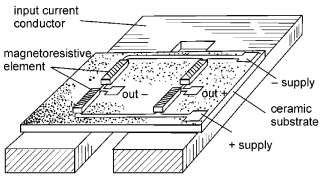

Fig. 2: Bridge-configured magnetoresistive current sensor [5].

are preferred for high-accuracy applications such as switch protection, recent improvements in open-loop designs have made them viable for compact and low cost systems [3].

B. Magnetoresistive Sensing Principles

Magnetoresistance is the change in electrical resistance of a ferromagnetic material in response to an external magnetic field [2]. Unlike Hall-effect sensing, which relies on charge motion, magnetoresistive effects arise from spin-dependent electron scattering. The electron's spin orientation relative to the material's magnetization affects scattering and thus the overall resistance [2]. To enhance sensitivity and reduce temperature drift, magnetoresistive elements are typically arranged in a Wheatstone bridge, as shown in Fig. 2 [6]. This structure increases signal output and enables thermal compensation [5]. A limitation of magnetoresistive materials is that these materials can retain a minor amount of magnetic memory after large current surges, which can slightly reduce the DC dynamic range [5]. The characteristics of magnetoresistive sensors depend on their structure and sensing mechanism.

1) **TMR:** Resistance changes as electrons tunnel between ferromagnetic layers through an insulating barrier [2].
2) **AMR:** Resistance varies with the angle between current flow and magnetization [2].
3) **GMR:** Resistance changes due to spin-dependent scattering in multilayer films.

In this paper, we focus only on TMR and AMR technologies, as GMR sensors were not available in our sensor portfolio.

1) Tunneling Magneto-resistive (TMR) Sensors: Due to their inherently highly sensitive way of detecting magnetic fields generated by current-carrying conductors, TMR sensors often deliver usable output voltage levels directly from the sensing bridge and therefore do not require additional signal amplification [7].

Similar to Hall-effect sensors, TMR sensors are also available in open-loop and closed-loop topologies. In closed-loop TMR sensors, a compensation coil generates a balancing flux to cancel the primary field. This allows operation in a zero-flux mode where the output reflects the measured current more accurately [7]. According to experimental results, a closed-loop TMR sensor operating in zero-flux mode achieved an average relative error of 0.31% over the AC 0–100 mA range, with an r value of 1.0 [7]. These results highlight the potential of the technology for high linearity, high precision, and high sensivity under the weak current of both AC and DC [2].

2) Anisotropic Magneto-resistive (AMR) Sensors: It relies on resistance changes caused by variations in the angle between electric current and magnetization in a ferromagnetic material.

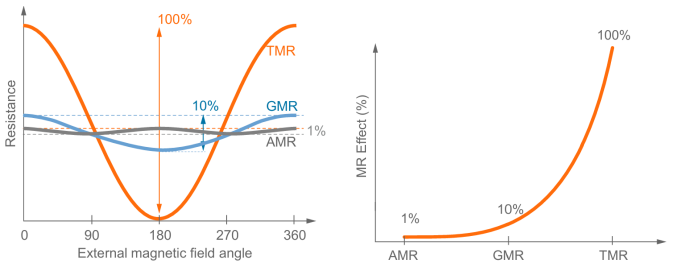

(a) Signal Amplitude Comparison (b) Relative MR effect.

Fig. 3: Comparison of magneto resistive technologies [2].

While AMR offers certain advantages, it is inherently nonlinear and temperature-sensitive. To overcome these limitations, commercial AMR sensors use magnetic field shaping and closed-loop feedback to reduce temperature drift and external interference for better stability and precision [2], [5].

Figures 3a and 3b illustrate the differences in signal amplitude among magneto-resistive technologies. TMR exhibits higher resistance sensitivity, with up to 100%, significantly outperforming AMR. Another advantage of TMR over AMR is its ability to sense magnetic fields across a full 360° rotation, which is beneficial in angular and position sensing applications.

III. Sensor Portfolio and Specifications

A set of magnetic current sensors was chosen and tested using Hall-effect, TMR, and AMR technologies for comparison (see Table I. These sensors cover nominal current ratings from ±5 A to ±90 A and support bidirectional measurement of AC and DC currents. They are all operated with single-ended analog outputs.

The Hall effect sensors and TMR sensor from the Allegro Microsystems, as well as the AMR sensors from ACEINNA were tested using their own evaluation boards [8] [9] [10] [11] [12]. Furthermore, a custom 4-layer PCB was developed for Sensitec CAS5000 series TMR sensors [13] and is described in detail in Section IV.

IV. Custom PCB for Current Sensing

As part of this study, a custom analog current sensing PCB was developed to interface between a three-phase inverter and the ADC acquisition stage within the UltraZohm control platform. The board serves as a dedicated solution for isolated, high-voltage current measurement, specifically designed for evaluating Sensitec CAS5000-series closed-loop TMR sensors.The board design supports isolation between current-carrying phases.

The PCB features four independent current measurement channels, each with a dedicated CAS5000-series sensor, differential amplifier stage, and output pair routed to an RJ45 Ethernet connector. The input current is fed through press-fit REDCUBE terminals, allowing continuous currents up to 130 A [14].

Each signal is conditioned using a THS4521 fully differential op-amp stage [15], referenced to a precision 2.5 V voltage reference IC (REF35250) [16]. This architecture is suited for differential ADC acquisition.

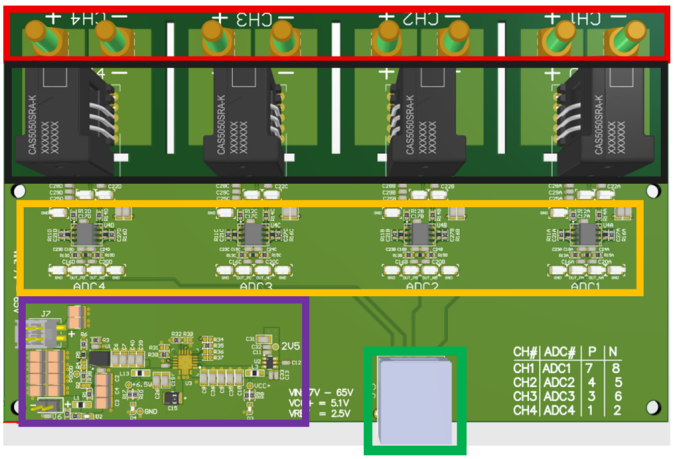

Fig. 4: 3D layout view of the custom 4-layer current measurement PCB with color highlighted key blocks: Current input terminals (red), Sensitec sensors (black), differential amplifiers (yellow), power supply circuitry (purple) and Ethernet signal outputs (green).

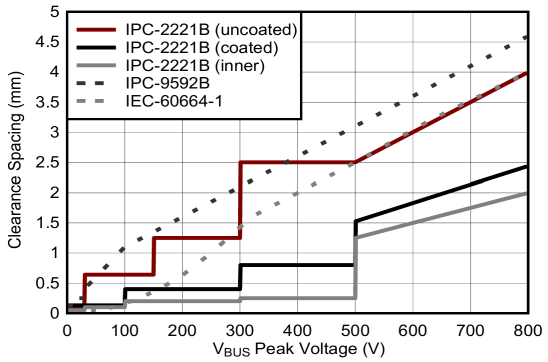

Fig. 5: PCB high-voltage clearance requirements as given by different standards [23].

The board accepts a wide input supply (7–65V) and features DC/DC power conversion including a TPSM365R3 integrated buck regulator power module [17] and a TPS7A47 LDO [18] All four channels are physically isolated. Thermal tests showed surface temperatures up to 100°C under 120 A DC per phase, practically setting the upper current limit.

V. Voltage Rating Constraints

To determine the safe maximum phase-to-phase voltage rating of the custom PCB, relevant insulation industry standards were reviewed: IEC 60664-1 (most conservative) [19], IEC 61800-5-1 [20], IPC-9592B [21], and IPC-2221B (least conservative) [22]. These standards define the minimum creepage and clearance distances required to maintain electrical insulation in high-voltage AC operation.

A. Voltage Rating Based on Clearance

Figure 5 compares high voltage clearance requirements from various industry standards. Among them, IEC 60664-1 requires the largest minimum spacing at a given voltage. For example, it specifies 4.5 mm clearance at 800 V_{Peak}, while IPC-2221B allows as little as 2.5 mm for coated boards at the same voltage level. This custom PCB has 9 mm clearance between sensor phases which means it exceeds even the IEC 60664-1 requirement comfortably.

B. Voltage Rating Based on Creepage

In accordance with IEC 60664-1, insulation design on PCBs must also consider the environmental conditions, characterized by the pollution degree and the material group. The material group is determined by the Comparative Tracking Index (CTI), which reflects a material's resistance to surface tracking. FR4, the most commonly used PCB substrate, has a CTI typically between 175 and 250, classifying it as Material Group IIIa. For typical industrial applications in Pollution Degree 2 environments, this classification requires more conservative creepage distances. For instance, a 400 V_{RMS} working voltage requires 4 mm of creepage for insulation, and 10 mm is required for 1000 V_{RMS} as summarized in IEC 60664-1 Table F.4. In total, aligned with the strictest interpretation of clearance and creepage limits, the high voltage custom PCB can be safely rated for a maximum phase-to-phase working voltage of 1000 V_{RMS} [23].

VI. Experimental Methods

A. DC Output Characterization

To evaluate the static performance behavior of the sensors, a set of DC measurements was performed using EA-PSB 10060-340 power supply and a KEYSIGHT 34461A Digit multimeter. Each sensor was tested in its nominal current range applying known DC currents and recording the analog output voltage (V_{out}) and the reference voltage (V_{ref}). The current sweep was performed with finer steps near 0 A and coarser steps at higher currents.

To evaluate the DC performance of each sensor, a linear model of the form was fitted to the data from each sensor using (1). G is the fitted gain in mV A^{-1} and b is the offset voltage at 0 A. The nominal gain values $G_{\text{theoretical}}$ from datasheet are listed as a reference.

$$V_{\text{out}} = G \cdot I_{\text{in}} + b \tag{1}$$

The linearity error r was calculated for each sensor using (2) to quantify the linearity. This metric is defined as the ratio of the maximum absolute deviation $\Delta L_{\max}$ between the actual sensor output and the linear fit, to the full-scale sensor output y_{FS}. The closer the value of r is to zero, the better the linear characteristics of the sensor output [24]. Here, y_{FS} was calculated using the measured gain a_{meas} so that r reflects deviations relative to the sensor's actual output span observed during testing, rather than idealized datasheet values[1].

$$r = \pm \frac{\Delta L_{\max}}{y_{\text{FS}}} \times 100\% \tag{2}$$

[1]While datasheet definitions of total output error (e.g., in [8]) calculate deviation relative to the ideal voltage based on nominal sensitivity, the analysis in this work uses a linear regression model fitted to the measured data for a direct comparison of sensors under real conditions. The datasheet error model provides a more specification-driven view, while the curve-fitted approach shows the actual sensor behavior.

TABLE I: Summary of DC Test Results for Current Sensors (with Accuracy Calculation)

	Datasheet			Measured/Calculated				
Sensor	f_{BW} (Hz)	I_{ND} (μA/$\sqrt{\text{Hz}}$)	$G_{\text{theoretical}}$ (mV/A)	G_{measured} (mV/A)	b (V)	$\Delta L_{\max}$ (mV)	r (%)	ε_{acc} (%)
Open-Loop Hall-Effect Sensors (Allegro). Package: SOICW-16								
ACS37002LMABTR-050B5-M	400k	350	40.0	36.1	2.502	8.3 @ −35 A	0.23	11.63
ACS37002LMCATR-090B5	400k	350	22.2	21.7	2.4999	5.4 @ −3 A	0.138	3.08
Open-Loop AMR Sensors (Aceinna). Package: SOICW-16								
MCA1101-5-5	1.5M	10	350.0	333.4	2.1983	−91.0 @ −4 A	−2.73	7.50
MCA1101-20-5	1.5M	10	90.0	89.6	2.1796	−13.6 @ −2 A	−0.38	1.06
MCA1101-50-5	1.5M	10	35.0	34.7	2.1777	42.7 @ 50 A	1.23	2.37
Open-Loop TMR Sensor (Allegro). Package: SOICW-16								
CT432-HSWF50MR	1M	44.3	40.0	39.9	2.501	7.9 @ 4 A	0.198	0.52
Closed-Loop TMR Sensors (Sensitec). Package: THD-8 (KH)								
CAS5050SRA-KH	400k	N/A	12.5	12.5	2.4933	−1.7 @ 50 A	−0.136	0.32
CAS5075KRA-KH	400k	N/A	6.25	6.22	2.501	−1.7 @ 75 A	−0.182	0.35

Furthermore, to quantify the total accuracy of the measurement, the overall accuracy error ε_{acc} was calculated by summing the gain error ε_G, r, and the offset error, calculated as (3). V_{ref} is the ideal reference voltage according to datasheet. At high current levels, the ε_{acc} will be dominated by the Gain error and r, whereas at low current, the dominant characteristic is the offset error [8]. Table I summarizes the results for all sensors, including their bandwidths and noise density values from the datasheets.

$$\varepsilon_{\text{acc}} = \underbrace{\left|\frac{G_{\text{measured}} - G_{\text{theoretical}}}{G_{\text{theoretical}}}\right| \times 100\%}_{\text{Gain error}} + \underbrace{|r|}_{\text{Linearity error}} + \underbrace{\left|\frac{b - V_{\text{ref}}}{y_{\text{FS}}}\right| \times 100\%}_{\text{Offset error}} \quad (3)$$

Overall, TMR sensors showed superior DC performance compared to Hall-effect and AMR technologies, with closed-loop TMR sensors performing slightly better than their open-loop counterparts. Among the three Aceinna AMR sensors, the MCA1101-20-5 provided the most accurate and symmetric output, centered around its nominal reference voltage of 2.175 V. In contrast, the MCA1101-5-5 showed the poorest performance. Despite their higher current ratings, the 20 A and 50 A variants outperformed the 5 A version even in lower current ranges. For the Allegro Hall-effect sensors, both variants maintained a stable reference voltage near 2.5 V. The ACS37002LMCATR-090B5 exhibited much higher overall accuracy than the 50 A version. All in all, the TMR sensors (CT432-HSWF50MR, CAS5050SRA-KH, CAS5075KRA-KH) delivered the lowest combined gain, offset, and linearity errors.

As noted in Section II-B, TMR sensors detect magnetic field-induced resistance changes directly, which results in better linearity and lower sensitivity to thermal effects. In contrast, Hall-effect sensors require internal signal amplification making them more susceptible to temperature-related gain drift. During high-current measurements, it was observed that TMR and AMR sensors exhibited negligible temperature drift, whereas Hall-effect sensors showed noticeable drift.

B. Time- and Frequency-Domain Observations

To evaluate the ripple characteristics and internal modulation behavior of different current sensor technologies, a 0.5 A_{RMS}, 1 kHz sinusoidal current was applied to each sensor and their output responses are observed. The differential output voltage was measured with single-ended oscilloscope probes relative to VV_{ref}, capturing the raw, unfiltered sensor output. Each channel was post-processed by dividing by the gain as listed in Table I. Thus, normalized current-equivalent waveforms are obtained for direct and fair comparison.

Figures 6 show both time-domain waveforms and their corresponding FFT spectra across the sensors. The FFT reveals the frequency components that make up the observed ripple in the time domain. This allow identification of dominant noise contributors, such as internal modulation tones or broadband amplification noise. In general, narrow-band spikes in the FFT correspond to periodic ripples, while elevated noise floors indicate broadband interference or internal switching artifacts. It should also be indicated that the sensors vary in bandwidth (see Table I. These bandwidth limits define the sensor's ability to follow rapid signal changes and attenuate high-frequency components. Consequently, bandwidth affects both ripple suppression and spectral noise behavior in the measured output [25].

Upon comparing the waveforms, the CT432-HSWF50MR (yellow) and MCA1101-50-5 (red) sensors exhibit flat FFT spectra with minimal spectral content, indicating low broadband noise and minimal ripple in the time-domain response. The CAS5050SRA-KH (blue) shows a slightly elevated noise floor up to its bandwidth limit (400 kHz), after which the spectral magnitude drops. In contrast, the CAS5075KRA-KH (orange) exhibits significantly higher broadband noise, which is clearly reflected in its noisy time-domain output. The Hall-effect sensors display both elevated noise floors and multiple spectral spikes, particularly pronounced for the ACS37002-090B5 (green). For both Hall-effect models, a dominant internal modulation tone is observed around 973 kHz. These observations confirm that sensors with flatter noise floors and fewer harmonic peaks yield cleaner analog outputs, while higher broadband noise and internal modulation components contribute to increased ripple and degraded signal quality in time-domain measurements.

The FFT results are consistent with the noise characteristics specified in the datasheets. Sensors such as the CT432-HSWF50MR and MCA1101-50-5, which exhibited flat spectra and clean time-domain waveforms, correspond to lower I_{ND} values in Table I. In contrast, the ACS37002 Hall-effect sensors showed elevated noise floors and periodic spectral tones, reflecting their higher noise levels. Overall, the MCA1101-50-5 (AMR) and CT432-HSWF50MR (TMR) sensors demonstrated the impoved noise performance and signal clarity, while open-loop Hall-effect sensors exhibited higher noise.

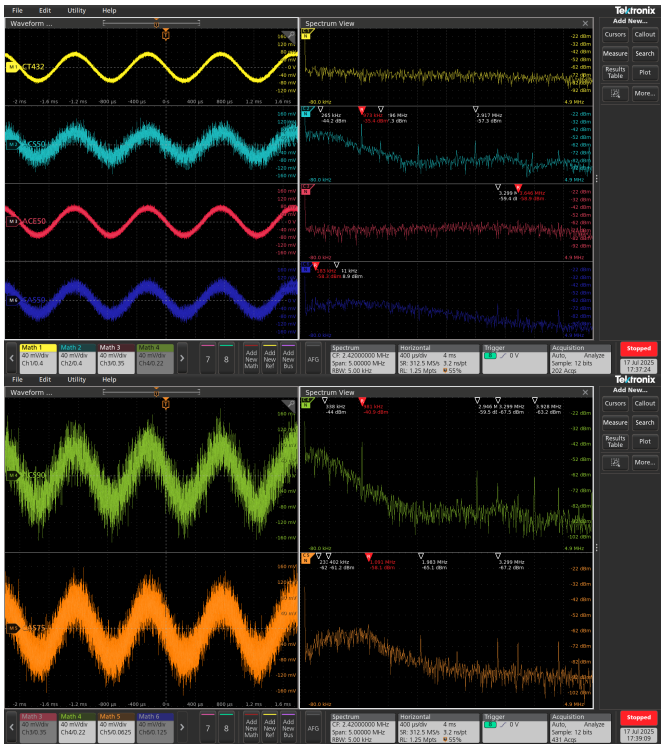

Fig. 6: Time- and frequency-domain observations of CT432-HSWF50MR (yellow), ACS37002LMABTR-050B5-M (cyan), MCA1101-50-5 (red), CAS5050SRA-KH (blue), ACS37002LMCATR-090B5 (green) and CAS5075KRA-KH (orange) under 0.5 A_{RMS}, 1 kHz sinusoidal current input.

C. AC Impedance Measurement

To characterize the dynamic impedance of the sensors, frequency-dependent measurements were performed using a Bode 100 vector network analyzer. A sinusoidal voltage from the Bode 100 is amplified by the Spitzenberger APS 1000 and converted into a current that is injected into the sensor's primary side. The resulting current and output voltage are captured by CH1 (via a Micsig CP1003B current probe) and CH2 (via Tektronix TPP0101 voltage probe) respectively. The impedance is then calculated using the equation (4).

$$Z(f) = \frac{V_{\text{out}}(f)}{I_{\text{in}}(f)} = \frac{V_{\text{CH2}}(f)}{V_{\text{CH1}}(f)} \tag{4}$$

However, the APS 1000 has a frequency-dependent current output that limits the usable bandwidth for impedance measurement. According to the manufacturer, the large-signal bandwidth

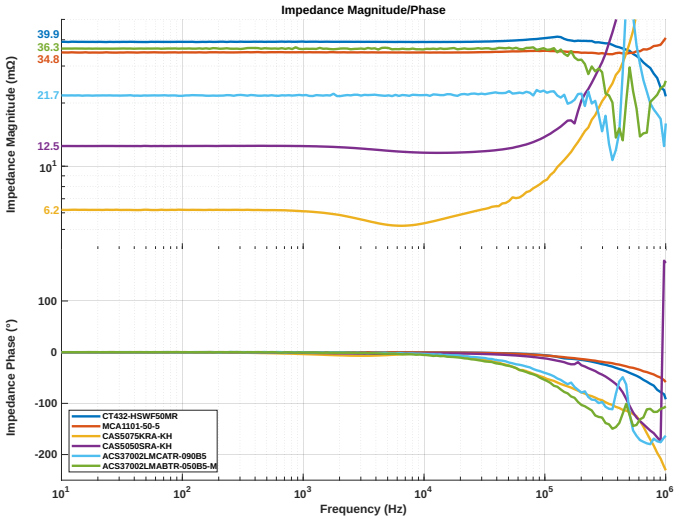

Fig. 7: Bode diagram showing impedance magnitude and phase response of tested sensors under a sinusoidal current input of 1.175 A_{RMS}.

(full-scale current) is limited to 10 kHz, while the small-signal bandwidth (10% of full-scale) extends up to 50 kHz at the −3 dB point [26]. As a result, impedance measurements beyond 50 kHz are considered unreliable due to reduced current output of the test setup, which leads to overestimated impedance values. The resulting Bode diagrams for all sensors are presented in Figure 7.

The impedance magnitude at the start of the frequency sweep (10 Hz), which is manually marked on the plot using coloured labels, closely matches the measured gains obtained from the DC linear regression model shown in equation (1)(Table I). Over the frequency range, the CT432-HSWF50MR and MCA1101-50-5 sensors exhibit a flat and stable magnitude response, whereas the Hall-effect sensors show minor instability seen as sharp local zigzag variations. These frequency-dependent gain fluctuations are characteristic of Hall-effect sensors and are not observed in other sensor technologies.

The phase response begins to decay around 10 kHz for sensors with a 400 kHz bandwidth, and around 100 kHz for sensors with bandwidths exceeding 1 MHz. In closed-loop control applications such as current regulation in inverters, this phase shift translates into a reduced control bandwidth and delayed response to fast transients [27].

A distinct dip in impedance magnitude is observed near 2 kHz for the Sensitec closed-loop TMR sensors, more pronounced for the CAS5075KRA-KH. This dip is attributed to an internal transition from closed-loop, field-sensor-controlled operation to a transformer-like behavior at higher frequencies. Although the winding ratio remains constant, this transition region introduces a visible drop in gain, which was described as a "turbo lag" effect by the manufacturer. Overall, the sensors CT432-HSWF50MR and MCA1101-50-5 with flat impedance and minimal phase shift demonstrated better dynamic stability.

VII. Conclusion

This work presented a comparative evaluation of Hall-effect, AMR, and TMR-based current sensors. Three key performance aspects were assessed: DC accuracy, time-domain ripple behavior, and AC impedance response.

In terms of DC output linearity and accuracy, the TMR sensors, particularly the closed-loop, outperformed their counterparts with superior gain precision and offset stability. In contrast, open-loop Hall-effect sensors showed larger gain errors and asymmetric behavior. Time-domain and FFT analyses further confirmed the low-noise characteristics of AMR and open-loop TMR devices. This was evidenced by their minimal broadband noise floor and flat FFT response indicating low spectral ripple. Hall-effect sensors suffered from elevated noise floors and internal modulation spikes. Lastly, AC impedance measurements revealed smooth and stable frequency responses for the CT432-HSWF50MR and MCA1101-50-5 sensors.

Sensitec's closed-loop TMR devices showed different behaviors. The CAS5050SRA-KH performed consistently well across all tests, with only a slight gain dip around 2 kHz due to internal operating mode transitions. In contrast, the CAS5075KRA-KH exhibited high broadband noise and degraded dynamic response despite its excellent DC linearity. This highlights the need to evaluate individual sensor variants, even within the same technology and product family.

Overall, AMR and TMR sensors demonstrated better linear behavior under static conditions, lower noise, cleaner FFT profiles, and improved impedance characteristics which make them more suitable for high-current, fast-switching applications such as motor control with SiC inverters.

References

[1] P. Niklaus, D. Bortis, and J. W. Kolar, "High-Bandwidth High-CMRR Current Measurement for a 4.8 MHz Multi-Level GaN Inverter AC Power Source," in *Proc. of the IEEE Applied Power Electronics Conference and Exposition (APEC)*, 2021.

[2] Allegro Microsystems, "From Hall Effect to TMR: A Comparison of Magnetic Sensing Technologies," Application Note AN117, 2023. [Online]. Available: Download PDF

[3] Allegro Microsystems, "Achieving Closed-Loop Accuracy in Open-Loop Current Sensors," [Online]. Available: Download PDF

[4] Bob Mammano, *Current Sensing Solutions for Power Supply Designers*, Unitrode/Texas Instruments Power Supply Design Seminar SEM1200, Topic 1, Document Number SLUP114, 1997.

[5] H. Kirkham, "Current Measurement Methods for the Smart Grid," in *IEEE Power Engineering Society General Meeting*, 2009.

[6] S. C. Mukhopadhyay and R. Y. M. Huang, *Sensors*. Berlin, Germany: Springer-Verlag, 2008, pp. 23–43.

[7] H. Deng, F. Huang, J. Guo, and H. Huang, "High Precision Closed-loop TMR Current Sensor for Small Current Measurement," in *Proc. 5th Int. Acad. Exchange Conf. on Science and Technology Innovation (IAECST)*, pp. 1402–1407, 2023, doi: 10.1109/IAECST60924.2023.10503169.

[8] Allegro Microsystems, *CT432: XtremeSense TMR Current Sensor*, Rev. 2, Nov. 2023. [Online]. Available: Download PDF

[9] Allegro Microsystems, *ACS37002: High Accuracy, Low Noise, Hall-Effect Current Sensor IC*, Rev. 1.0, 2021. [Online]. Available: Download PDF

[10] Allegro Microsystems, *ACSEVB-MC16 Evaluation Board User Guide*, August 2023. [Online]. Available: Download PDF

[11] ACEINNA Inc., *MCx1101 EVB User Manual*, Version 1.3, 2021. [Online]. Available: https://www.aceinna.com/current-sensors/evb

[12] ACEINNA, *MCA1101-xx-5 Current Sensor Datasheet*, Rev. L, Document 6020-1102-01, June 2024. [Online]. Available: https://www.aceinna.com

[13] Sensitec GmbH, *CAS5000-Series Datasheet: MagnetoResistive Current Sensor Module*, Document DSE_01, Rev. 02/2022. [Online]. Available: Download PDF

[14] Würth Elektronik eiSos GmbH & Co. KG, *WP-SHFU REDCUBE Press-Fit Terminal 7461001 Datasheet*, Version 3.0, June 2023. [Online]. Available: https://www.we-online.com/catalog/en/article/7461001

[15] Texas Instruments, "THS4521 Low Noise, Rail-to-Rail Output Fully Differential Amplifier," Datasheet, Rev. G, July 2023. [Online]. Available: https://www.ti.com/product/THS4521

[16] Texas Instruments, "REF35250 Precision 2.5-V Voltage Reference," Datasheet, Rev. D, Oct. 2023. [Online]. Available: https://www.ti.com/product/REF35250

[17] Texas Instruments, "TPSM365R3 65-V, 0.3-A Step-Down Power Module with Integrated Inductor," Datasheet, Rev. A, June 2024. [Online]. Available: https://www.ti.com/product/TPSM365R3

[18] Texas Instruments, "TPS7A47 1-A, Ultra-Low-Noise, High PSRR, Low-Dropout Linear Regulator," Datasheet, Rev. I, Apr. 2023. [Online]. Available: https://www.ti.com/product/TPS7A47

[19] IEC, *IEC 60664-1: Insulation Coordination for Equipment within Low-Voltage Supply Systems – Part 1: Principles, Requirements and Tests*, Geneva, Switzerland, May 2020.

[20] IEC, *IEC 61800-5-1: Adjustable Speed Electrical Power Drive Systems – Part 5-1: Safety Requirements – Electrical, Thermal and Energy*, Geneva, Switzerland, Aug. 2022.

[21] IPC, *IPC-9592B: Requirements for Power Conversion Devices for the Computer and Telecommunications Industries*, Bannockburn, Illinois, Jan. 2013.

[22] IPC, *IPC-2221B: Generic Standard on Printed Board Design*, Bannockburn, Illinois, Nov. 2012.

[23] W. Zhang and T. LaBella, "Demystifying Clearance and Creepage Distance for High-Voltage End Equipment," Texas Instruments Power Supply Design Seminar, Topic 2, Literature No. SLUP419, 2024. [Online]. Available: https://www.ti.com/lit/pdf/slup419

[24] M. Lei, T. Peng, F. Zhou, J. Yu, S. Liang, J. Liu, and L. Li, "Optimal design and implementation of tunnelling magnetoresistance based small current sensor with temperature compensation," *Energy Reports*, vol. 8, pp. 137–146, 2022. [Online].

[25] M. Cerna and A. F. Harvey, "The Fundamentals of FFT-Based Signal Analysis and Measurement," National Instruments Application Note 041, 2000. [Online]. Available: https://www.sjsu.edu/people/burford.furman/docs/me120/FFT_tutorial_NI.pdf

[26] Spitzenberger & Spies, *APS 1000 Current Amplifier Overview*, T&D Power Series Datasheet, Rev. 1107-e-0008-1. [Online]. Available: Download PDF

[27] B. Zhang, "Common time-delay compensation techniques for grid-connected inverters," in *Proceedings of Power Electronics and Motion Control Conference*, 2015. [Online]. Available: Wiley IET Digital Library.